Supporting Information

Kim et al. 10.1073/pnas.1314345110

SI Text

Biologically Derived Melanin Anodes Do Not Contain Significant Amounts of Exogenous Proteins

Both X-ray photoelectron spectroscopy (XPS) (Fig. S3) and Raman spectra (Fig. 2) confirm that there is a negligible amount of proteins present in the melanin anodes composed of biologically derived materials. First, amide bonds should produce prominent peaks in the Raman spectra in Fig. 2 between wave numbers of 1,630 and 1,680 cm^{-1}. These peaks would be associated with carbonyl stretches within amide bonds (1). However, these peaks are largely absent from Raman spectra recorded for naturally occurring eumelanins isolated from *Sepia officinalis* (NatMel), synthetic eumelanins prepared from autooxidation of tyrosine (SynMel), and synthetic melanin-like materials (E-SynMel). Furthermore, incorporating this additional peak into the composite signal produced unsatisfactory fits. The presence of residual proteins should produce a sulfur peak (corresponding to cysteines) in the XPS survey spectrum at ∼162–168 eV. However, this peak is absent in the spectra for all three types of melanins used in this study.

Detailed Characterization of Melanin Anode Chemistry and Structure

Brunauer–Emmett–Teller Method for Surface Area Analysis. The surface area calculations derived from Brunauer–Emmett–Teller (BET) measurements suggest that the overall specific surface area of melanin materials used in this study (19.9 $m^2\ g^{-1}$) is comparable to previous reports of 21.5 $m^2\ g^{-1}$ (2). All three melanin compositions follow a type IV behavior as characterized by the presence of a rounded knee at low values of p/p_o and a small slope at intermediate values of p/p_o. These features correspond to the formation of monolayers and multilayers, respectively. The small values of absorbed volumes V at low normalized pressures p/p_o for all melanin compositions suggest that there is limited surface area for monolayer adsorption. This observation is consistent with the calculated specific areas. Another notable feature for the BET measurements is the significant hysteresis observed in SynMel and E-SynMel, but not NatMel. These data suggest that both SynMel and E-SynMel are composed of disordered networks, which is corroborated by SEM micrographs (Fig. 1). BET and Barrett–Joyner–Halenda (BJH) data sets recorded in this work also suggest NatMel is composed of nanometer-scale textured granules.

BJH Method. Finally, the data produced from the BJH method offer additional insight into the different mesoporous structures of the three melanin compositions used in this study. Before this discussion, it is important to comment on the methods used in the preparation of the three distinct melanin compositions. NatMel is a natural pigment that is isolated from *S. officinalis*. It is an extended heterogeneous biopolymer composed of 5,6-dihydroxyindole (DHI) and 5,6-dihydroxyindole-2-carboxylic acid (DHICA), aromatic bicyclic monomers that are coupled to each other at the 2, 4, and 7 positions through a variety of permutations. DHI and DHICA precursors form tetramers that assemble into multilayers through strong π–π interactions. Furthermore, multilayers form concentric rings that build up to form isotropic homogeneous nanoparticles that agglomerate into larger superstructures (3). The SynMel used in this study is prepared from oxidative polymerization of L-tyrosine. The sequential oxidation of L-tyrosine first produces a quinone, followed by cyclization of the 5-member ring via Michael addition, and finally oxidative polymerization at the 2, 4, and 7 positions. E-SynMel is prepared from oxidative polymerization of 5,6-dimethoxyindolecarboxylic acid (4).

Hence, both NatMel and E-SynMel are prepared through oxidative polymerization of bicyclic aromatics at the 2 (in the case of NatMel without carboxylic acid groups), 4, and 7 positions. These compositions exhibit pore-size distributions in which the dominant pore diameter is in the range of 3–4 nm. Therefore, these materials are classified as mesoporous (5). Pore-size distributions at this length scale (<5 nm) confer increased charge storage capacities (6). The preparation of SynMel in oxidative environments is a two-step process that requires cyclization of L-tyrosine followed by polymerization. However, it is possible that ring formation and oxidative polymerization proceed concurrently, which may lead to the incorporation of L-tyrosine at the 4 and 7 positions. Pendant primary amines may increase the porosity of the resulting network, which likely explains the shift in the pore-size distribution to larger diameters. These larger pore sizes may explain the reduced apparent sodium loading as measured by XPS data. The smaller fraction of sodium (as measured by atomic percent) may be an artifact that can be explained by sodium-ion loading into pores that cannot be directly measured due to the small characteristic penetration depth of XPS. This measured value of sodium is much smaller than that of NatMel and E-SynMel, which are exclusively mesoporous materials as assessed by BJH.

Thermogravimetric Analysis. Thermograms of pristine and Na^+-loaded melanin anodes materials are shown in Fig. S4. Melanins have been previously shown to be thermally stable up to temperatures of ∼200 °C (7). Between 200 and 800 °C, melanin-based materials undergo a monotonic reduction in mass (8). Data gathered in this study corroborate these previously reported observations. There are several other notable observations. The rate of mass loss is generally attenuated for Na^+-loaded melanin compared with the respective pristine melanin counterparts. These data suggest that the sodium loading increases the stability of the melanin materials. This phenomenon was previously observed in other aromatic anode materials with carboxylate groups (9). There are two nodes observed in the thermogram that occur at approximate temperatures of 480 and 590 °C across all three Na^+-loaded melanin compositions. These features correspond to compositions of melanin that are complexed with two different amounts of sodium ions. Sodium-loaded terephthalate-based anodes exhibited two distinct nodes at 320 and 640 °C, which correspond to monosodium terephthalate and disodium terephthalate compositions (9). Therefore, nodes that occur at higher temperatures arise due to the decomposition of melanin components that exhibit increased sodium loading. There are also more pronounced plateaus in weight loss between 480 and 590 °C for NatMel and E-SynMel compared with SynMel. This is likely due to the increased homogeneity of NatMel and E-SynMel compared with SynMel.

Detailed Comparison of Melanin Anode Performance Compared with Activated Carbon

Activated carbon (AC) is a suitable material to benchmark the performance of melanin-based anodes as charge storage materials. Aqueous-based supercapacitors that use activated carbon electrodes exhibit specific capacitances of 100–200 Fg^{-1}, which correspond to capacities of 25–55 $mAhg^{-1}$ operating at 1 V. Namely, AC can deliver about 30 $mAhg^{-1}$ if used in a neutral alkaline solution (10). Even though the mass-normalized capacity of melanin (10 m^2g^{-1}) is smaller than AC (2,000 m^2g^{-1}), melanin anodes exhibit higher capacity with respect to the real surface area based on faradaic (charge transfer) reactions.

1. Triggs NE, Valentini JJ (1992) An investigation of hydrogen bonding in amides using Raman spectroscopy. *J Phys Chem* 96(17):6922–6931.
2. Liu Y, Simon JD (2003) The effect of preparation procedures on the morphology of melanin from the ink sac of Sepia officinalis. *Pigment Cell Res* 16(1):72–80.
3. Watt AAR, Bothma JP, Meredith P (2009) The supramolecular structure of melanin. *Soft Matter* 5(19):3754–3760.
4. Povlich LK, Le J, Kim J, Martin DC (2010) Poly(5,6-dimethoxyindole-2-carboxylic acid) (PDMICA): A melanin-like polymer with unique electrochromic and structural properties. *macromolecules* 43(8):3770–3774.
5. Sing KSW, et al. (1985) Reporting physisorption data for gas/solid systems with special reference to the determination of surface area and porosity. *Pure Appl Chem* 57(4): 603–619.
6. Jung DS, Ryou M-H, Sung YJ, Park SB, Choi JW (2013) Recycling rice husks for high-capacity lithium battery anodes. *Proc Natl Acad Sci USA* 110(30):12229–12234.
7. Bothma JP, de Boor J, Divakar U, Schwenn PE, Meredith P (2008) Device-quality electrically conducting melanin thin films. *Adv Mater* 20(18):3539–3542.
8. Deziderio SN, Brunello CA, da Silva MIN, Cotta MA, Graeff CFO (2004) Thin films of synthetic melanin. *J Non-Cryst Solids* 338-340:634–638.
9. Park Y, et al. (2012) Sodium terephthalate as an organic anode material for sodium ion batteries. *Adv Mater* 24(26):3562–3567.
10. Amatucci GG, Badway F, Du Pasquier A, Zheng T (2001) An asymmetric hybrid nonaqueous energy storage cell. *J Electrochem Soc* 148(8):A930–A939.

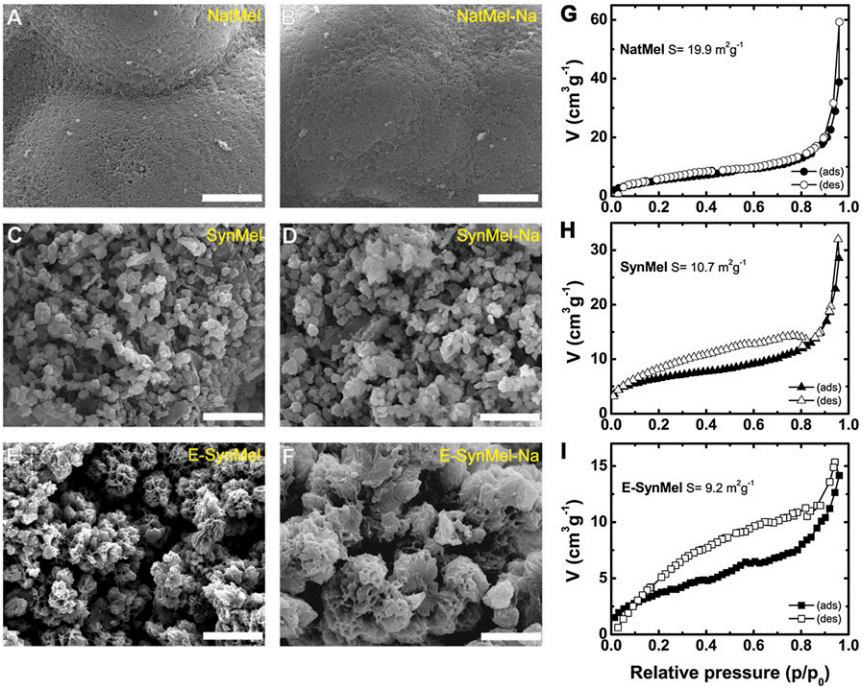

Fig. S1. SEM images of (*A*) pristine natural (NatMel), (*B*) Na^+-loaded natural (NatMel-Na), (*C*) synthetic (SynMel), (*D*) Na^+-loaded synthetic (SynMel-Na), (*E*) electrodeposited (E-SynMel), and (*F*) Na^+-loaded electrodeposited (E-SynMel-Na) melanins in low magnification. Scale bar, 3 μm. N_2 adsorption–desorption isotherms of (*G*) NatMel, (*H*) SynMel, and (*I*) E-SynMel.

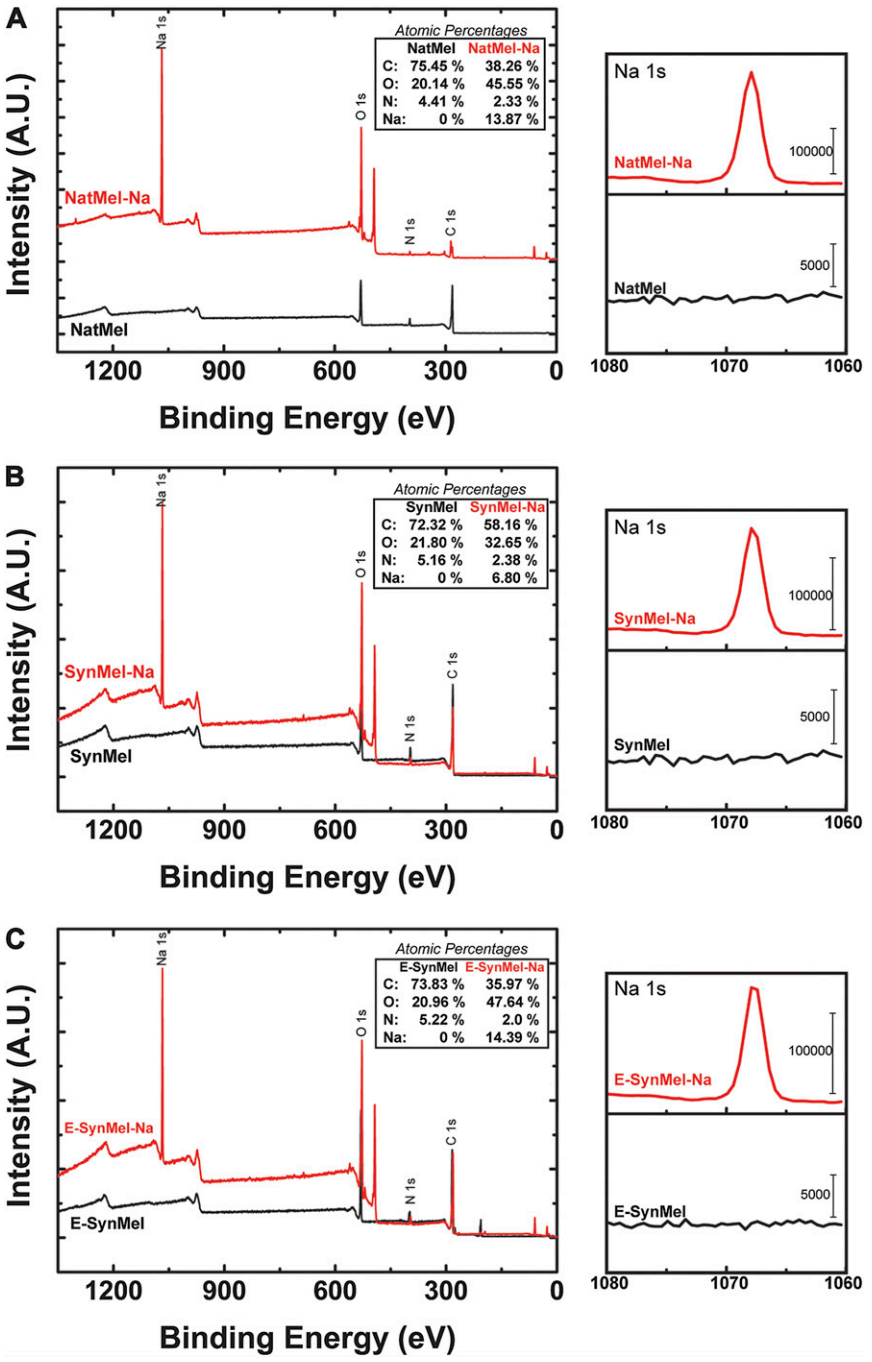

Fig. S2. XPS survey peaks of pristine and Na^{+}-loaded melanin anodes.

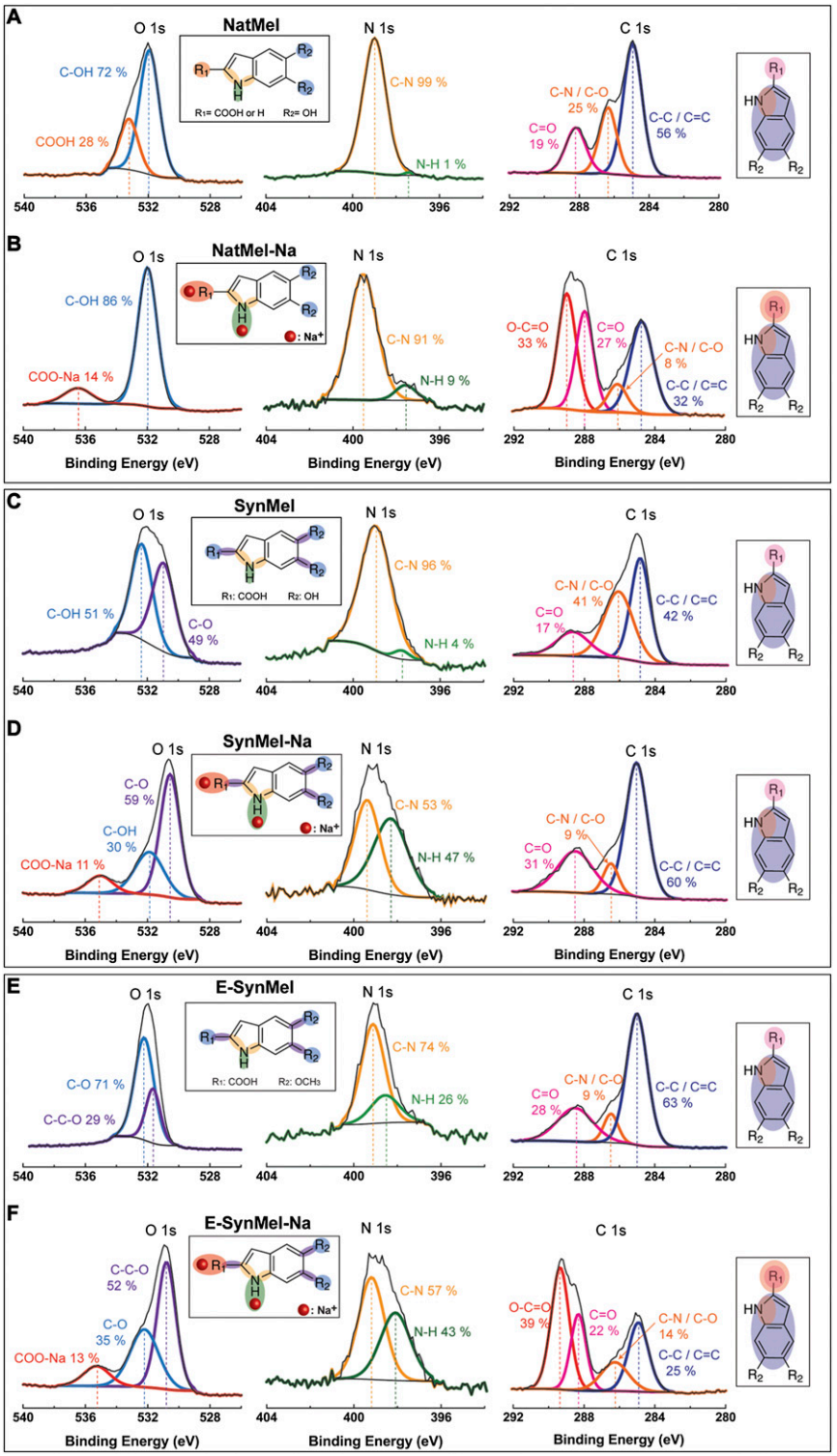

Fig. S3. High-resolution O 1s, N 1s, and C 1s XPS from pristine and Na^+-loaded melanins: (*A*) NatMel and (*B*) NatMel-Na; (*C*) SynMel and (*D*) SynMel-Na; and (*E*) E-SynMel and (*F*) E-SynMel-Na. Black lines represent the raw XPS spectra as recorded. Peak fitting and deconvolution was performed by CasaXPS and interpreted as colored lines with associated elemental analysis that are associated with the most likely bonding signatures.

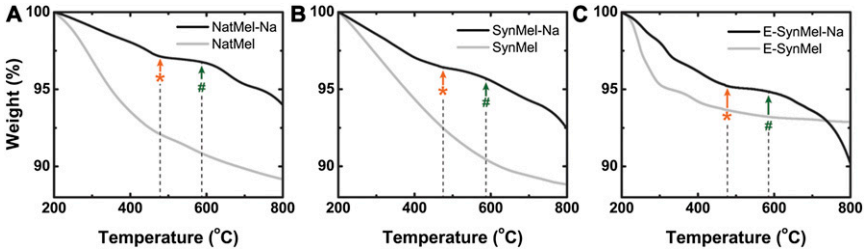

Fig. S4. Thermogravimetric analysis (TGA) of pristine and Na^+-loaded melanin anodes. Two representative phase transitions are shown by the symbols. These data suggest that sodium ions are bound to melanin anodes in multiple bonding configurations. TGA thermograms of E-SynMel indicate accelerated mass loss and the absence of well-defined transition compared with NatMel and SynMel. This suggests that the presence of aryl methoxy groups limits the extent of intermolecular hydrogen bonding and interferes with coordinated π–π stacking in E-SynMel protomolecules.

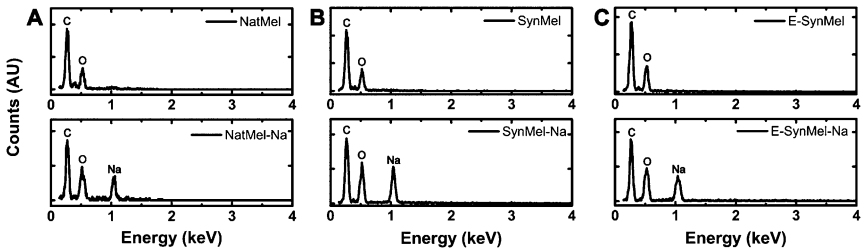

Fig. S5. Energy dispersive spectra of pristine and Na^+-loaded melanin anodes.

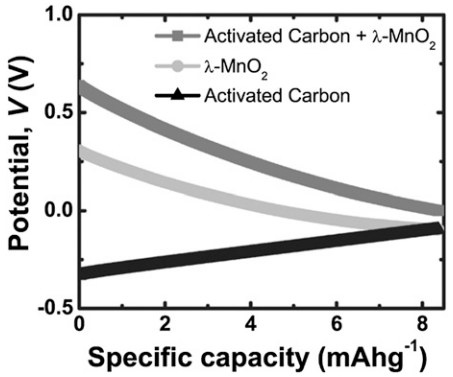

Fig. S6. Galvanostatic full cell discharge of Na^+-loaded activated carbon and λ-MnO_2 at −20 μA measured in 1 M Na_2SO_4 electrolyte. The specific capacity was measured by the mass of activated carbon anode.

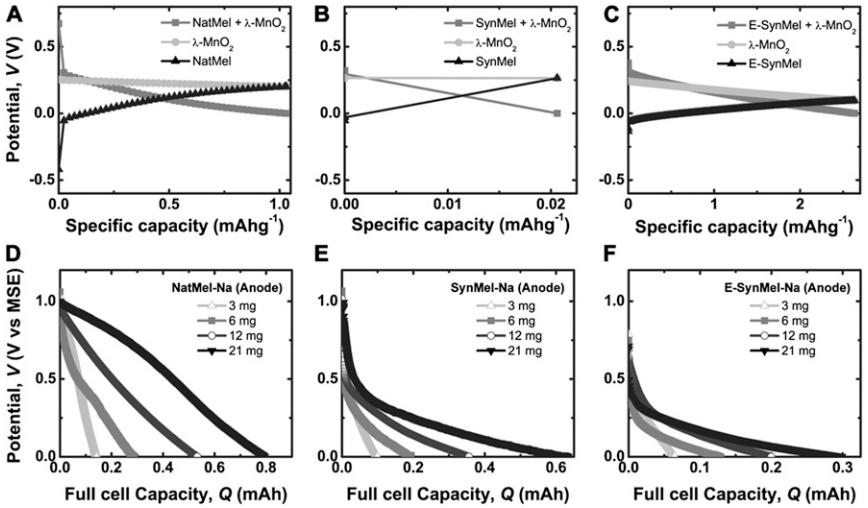

Fig. S7. Galvanostatic full cell discharge profiles of pristine melanin anodes: (*A*) NatMel, (*B*) SynMel, and (*C*) E-SynMel with λ-MnO_2 cathodes at rates of −10 μA in 1 M Na_2SO_4 electrolyte. The specific capacity of simple melanin anodes is significantly smaller compared with corresponding Na^+-loaded counterparts. (*D*–*F*) Galvanostatic full cell discharge profiles of λ-MnO_2 cathode and Na^+-loaded melanin anodes with varying mass at rates of −10 μA measured in 1 M Na_2SO_4 electrolyte. Melanin anodes with several absolute masses (3, 6, 12, and 21 mg) were used in combination with λ-MnO_2 cathodes of constant mass (8 mg).

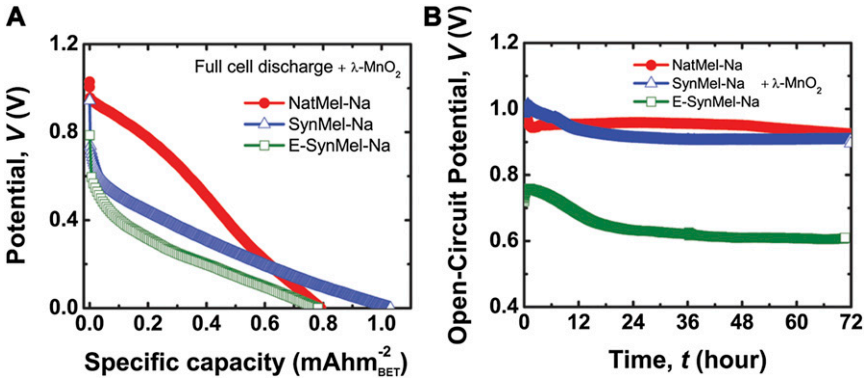

Fig. S8. Full cell discharge profiles of melanin anodes. (*A*) Specific capacities per surface areas ($mAhm^{-2}$) were calculated by specific capacities ($mAhg^{-1}$) divided by normalized surface areas ($m^2\ g^{-1}$) of each melanin material as measured by BET (Fig. 1). (*B*) Open-circuit potential of full cell made of Na^+-loaded melanin anodes and λ-MnO_2 cathodes. Potentials were measured in 1 M Na_2SO_4 electrolyte at 20 °C.

Table S1. Summary of high-resolution XPS analysis of melanin anodes

	Binding energy, eV		
Material	O 1s	N 1s	C 1s
NatMel	531.92 [C–OH]	397.42 [*N*–H]	284.93 [C–C]/[C=C]
	533.24 [COO–H]	398.99 [C–N]	286.35 [C–N]/[C–O]
			288.20 [C=O]
NatMel-Na	531.99 [C–OH]	397.08 [*N*–Na]	284.75 [C–C]/[C=C]
	536.46 [COO–Na]	399.03 [C–N]	286.13 [C–N]/[C–O]
			287.99 [C=O]
			289.00 [O–C=O]
SynMel	530.95 [C–O]	397.78 [*N*–H]	284.85 [C–C]/[C=C]
	532.34 [C–OH]	398.95 [C–N]	286.07 [C–N]/[C–O]
			288.65 [C=O]
SynMel-Na	530.54 [C–O]	398.30 [*N*–Na]	285.03 [C–C]/[C=C]
	531.87 [C–OH]	399.38 [C–N]	286.49 [C–N]/[C–O]
	535.04 [COO–Na]		288.50 [C=O]
E-SynMel	531.65 [C–C–O]	398.56 [*N*–H]	285.00 [C–C]/[C=C]
	532.21 [C–O]	399.12 [C–N]	286.47 [C–N]/[C–O]
			288.50 [C=O]
E-SynMel-Na	530.79 [C–C–O]	398.09 [*N*–Na]	284.92 [C–C]/[C=C]
	532.21 [C–O]	399.19 [C–N]	286.26 [C–N]/[C–O]
	535.28 [COO–Na]		288.32 [C=O]
			289.35 [O–C=O]

Table S2. Raman spectra of pristine and Na^+-loaded melanin anodes

Peak position, cm^{-1}								
NatMel	NatMel-Na	Shift Δ	SynMel	SynMel-Na	Shift Δ	E-SynMel	E-SynMel-Na	Shift Δ
1,227	1,192	−35	1,232	1,177	−55	1,198	1,173	−25
1,345	1,304	−41	1,351	1,314	−37	1,332	1,321	−11
1,442	1,431	−11	1,424	1,423	−1	1,410	1,417	+7
1,513	1,515	2	1,520	1,515	−5	1,507	1,513	+6
1,584	1,576	−8	1,589	1,579	−10	1,589	1,593	+11